



On the structural behavior of tapered thin-walled convex polygonal tubes with deformable cross-section

Rodrigo Gonçalves¹

Abstract

Tapered steel tubes with regular convex polygonal section are widely used in the construction sector, mostly as monopoles, to support lighting and telecommunication equipment, as well as overhead power lines. Such tubes are thin-walled and therefore susceptible to cross-section deformation. As a result, their structural analysis generally requires refined shell finite element models. This paper presents an alternative, namely a new Generalized Beam Theory (GBT) formulation for such tubes, able to carry out, very efficiently, first order and buckling (linear stability) analyses. The formulation is based on a “prismatic parent element” that is mapped to the true tapered configuration and thus can employ the cross-section deformation modes of the prismatic case. Even though the resulting equations are significantly involved due to taper effects, it is possible to enforce the standard GBT kinematic assumptions exactly, an aspect that is essential for the overall performance of the formulation. A relatively wide range of numerical examples is presented, to show that the finite element implementation of the proposed GBT can predict the linear and buckling behavior of tapered tubes with remarkable accuracy and computational savings with respect to shell finite element models, even for high taper angles.

1. Introduction

Regular (equiangular and equilateral) convex polygonal section (RCPS) tubes, commonly used in the construction industry as monopoles, exhibit very peculiar structural features owing to the cross-section rotational symmetry, of order equal to the number of sides, n . In particular, duplicate cross-section geometric/stiffness properties for global, distortional and local deformation modes are obtained. These mode pairs constitute a 2D space and any rotation in that space leads to the exact same geometric/stiffness property, a generalization of the fact that all central axes are principal bending axes. This feature leads to a peculiar and rich structural behavior, since the tube stiffness is invariant upon a rotation of the loads according to the cross-section symmetry, and buckling/vibration eigenvalues with a geometric multiplicity equal to 2 are obtained.

Generalized Beam Theory (GBT) is a thin-walled beam theory with an enriched kinematic description to allow capturing cross-section deformation. This theory, proposed by Schardt (1989) — see the bibliography listed at <https://vtb.info/> and <https://sites.fct.unl.pt/gbt/> —, is known for

¹ Full Professor, CERIS and Universidade Nova de Lisboa, Portugal <rodrigo.goncalves@fct.unl.pt>

its ability to obtain accurate solutions with a very low computational cost, while providing a unique insight due to the fact that the solution is expressed in terms of structurally meaningful so-called “cross-section deformation modes”. The specialization of GBT to prismatic RCPS tubes, which duly accounts for the cross-section rotation symmetry, and its application in linear and eigenvalue (buckling and vibration) problems was developed by Gonçalves & Camotim (2013a, 2013b, 2013c, 2014). Later, an enhanced geometrically non-linear GBT (Martins et al. 2018) was used to assess the post-buckling behavior of RCPS tubes (Martins et al. 2019a, 2019b, 2021).

This paper presents the extension of GBT to tapered RCPS tubes, a noteworthy development considering that the only GBT formulations available for genuinely tapered elements are for conical shells (Nedelcu 2011, Mureşan et al. 2019, Gonçalves & Nedelcu 2024), in which case the geometry is still somewhat simple, the strain-displacement relations are available from thin shell theory and the GBT deformation modes do not require the cross-section analysis procedure. The proposed approach and its finite element implementation are presented in Section 3, following a brief review of the kinematic description for the prismatic case in Section 2. A relatively wide range of first order and buckling (linear stability) numerical examples is presented and discussed in Section 4. For comparison and validation purposes, refined shell finite element results are provided. The paper closes in Section 5 with the main conclusions of the work carried out.

The GBT vector-matrix notation introduced previously (Gonçalves & Camotim, 2011) is followed. A comma indicates a derivative, but the prime denotes a derivative with respect to x . Matrices and vectors are represented by boldface letters.

2. The GBT kinematic description for prismatic RCPS tubes

First, the GBT kinematic description for prismatic RCPS tubes is briefly reviewed. The notation is as shown in Fig. 1(a). Using Kirchhoff’s thin plate assumption, the displacement vector for each wall, along the local axes (x, y, z) is written as

$$\mathbf{U} = \begin{bmatrix} U_x \\ U_y \\ U_z \end{bmatrix} = \begin{bmatrix} u(x, y) - zw'(x, y) \\ v(x, y) - zw_{,y}(x, y) \\ w(x, y) \end{bmatrix}, \quad \begin{cases} u = \sum_{k=1}^D \bar{u}_k(y) \phi'_k(x) = \bar{\mathbf{u}}^T(y) \boldsymbol{\phi}'(x), \\ v = \sum_{k=1}^D \bar{v}_k(y) \phi_k(x) = \bar{\mathbf{v}}^T(y) \boldsymbol{\phi}(x), \\ w = \sum_{k=1}^D \bar{w}_k(y) \phi_k(x) = \bar{\mathbf{w}}^T(y) \boldsymbol{\phi}(x), \end{cases} \quad (1)$$

where (u, v, w) are the mid-surface displacement components along the local axes, which are expressed in terms of $k = 1, \dots, D$ deformation modes, with displacement components $(\bar{u}_k(y), \bar{v}_k(y), \bar{w}_k(y))$ and amplitude functions $\phi_k(x)$. Furthermore, the boldface letters are column vectors that collect the matching letter k components. The deformation modes are calculated through the so-called “cross-section analysis”, which for arbitrary flat-walled cross-sections can be performed using the GBTUL software (Bebiano et al. 2015, 2018). For RCPS, due to the cross-section rotation symmetry, the procedure can be significantly optimized (Gonçalves & Camotim 2013a). The cross-section analysis starts with a cross-section discretization into n natural nodes (fold-lines) and m intermediate nodes in each wall, whose displacement DOFs (not rotations) are used to generate an initial basis, of dimension $3n(m + 1)$. The final basis, i.e. the deformation mode set, is obtained after a proper orthogonalization procedure. Fig. 1(b) shows an example obtained with GBTUL. Besides the bending modes 2-3, the distortional modes 5-6 also

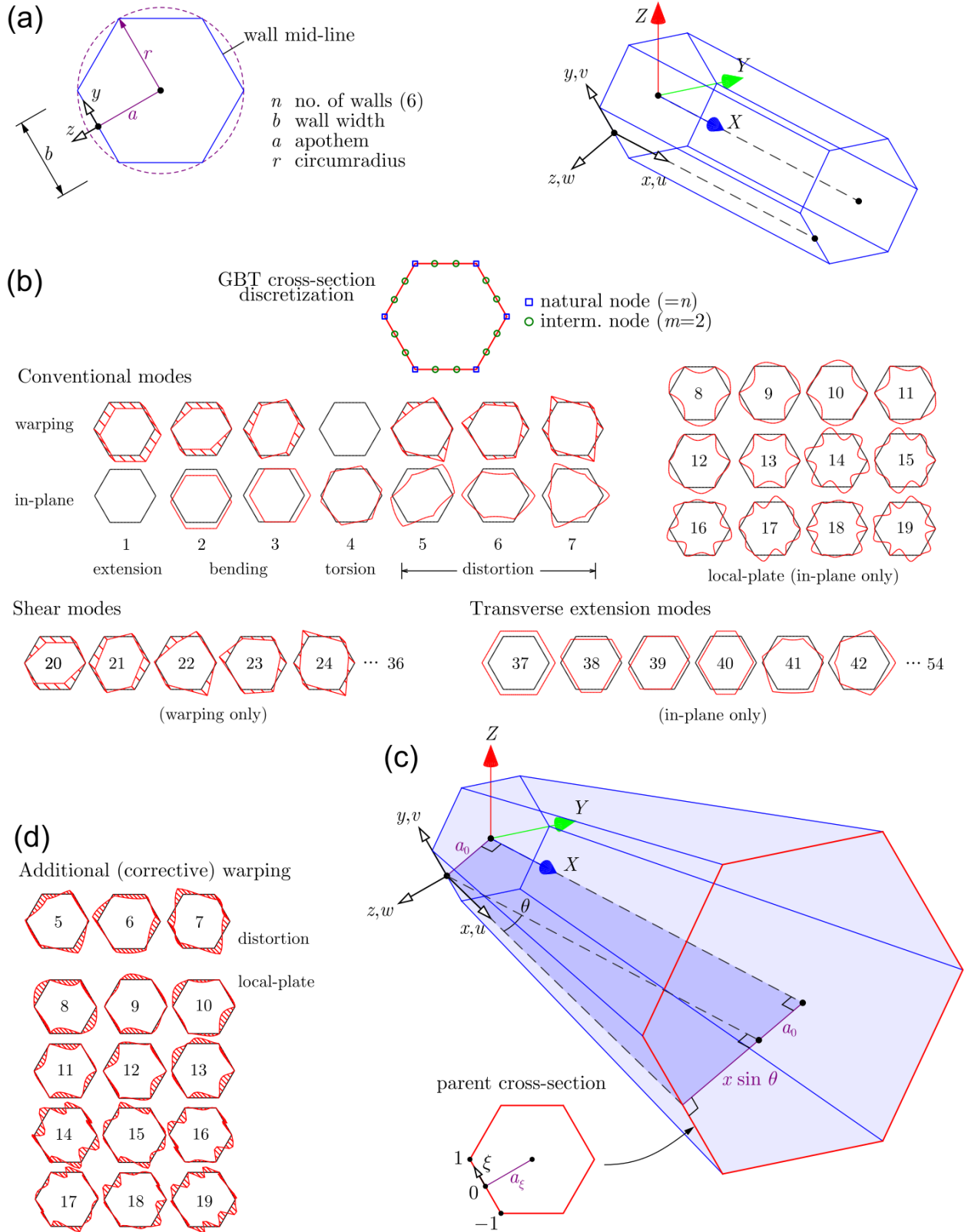


Figure 1: (a) Geometry, axes and displacement components for a prismatic tube. (b) GBT discretization and deformation modes. (c) Geometry, axes and displacement components for a tapered tube. (d) Additional warping modes.

constitute a pair (same cross-section geometric/stiffness properties). Some local modes also constitute pairs, but the GBTUL procedure does not allow their clear separation. It is worth remarking that the conventional mode subset generally suffices to obtain accurate solutions.

3. GBT formulation for tapered RCPS tubes

3.1 Kinematic description and strains

For tapered RCPS tubes, see Fig. 1(c), the variable apothem is given by $a(x) = a_0 + x \sin \theta$, where θ is the taper angle, and a “parent” cross-section is used, with the mid-line natural coordinate $\xi = 2y/b \in [-1,1]$ and corresponding apothem $a_\xi = \cot(\pi/n)$. In this approach, using the chain rule, for $f = f(\xi)$, the derivatives read

$$\begin{cases} f' = J_x f_{,\xi}, & J_x = -\frac{\xi \sin \theta}{a}, \\ f'' = J_{xx} f_{,\xi} + J_x^2 f_{,\xi\xi}, & J_{xx} = \frac{2\xi \sin^2 \theta}{a^2}, \\ f_{,y} = J_y f_{,\xi}, & J_y = \frac{2}{b}, \\ f_{,yy} = J_{yy} f_{,\xi} + J_y^2 f_{,\xi\xi}, & J_{yy} = 0, \\ f'_{,y} = J_{xy} f_{,\xi} + J_x J_y f_{,\xi\xi}, & J_{xy} = -\frac{a_\xi \sin \theta}{a^2}. \end{cases} \quad (2)$$

The deformation modes of the prismatic case can be used provided that the displacements are defined along axes (X, y, a) . The mid-surface displacements are in the tapered case given by

$$\begin{cases} U_x = \sum_{k=1}^D (\bar{u}_k(\xi) \varphi_k(x) + \tilde{u}_k(\xi) \phi_k(x)) = \bar{\mathbf{u}}^T \boldsymbol{\varphi} + \tilde{\mathbf{u}}^T \boldsymbol{\phi}, \\ U_y = \sum_{k=1}^D \bar{v}_k(\xi) \phi_k(x) = \bar{\mathbf{v}}^T \boldsymbol{\phi}, \\ U_a = \sum_{k=1}^D \bar{w}_k(\xi) \phi_k(x) = \bar{\mathbf{w}}^T \boldsymbol{\phi}, \end{cases} \quad (3)$$

which is similar to Eq. 1, although a new warping component \tilde{u}_k and amplitude function φ_k were introduced, to allow enforcing Vlasov’s assumption (null membrane shear strains). It is shown in Gonçalves (2024) that these new terms are not independent, being given by

$$\varphi_k = \frac{\phi'_k}{J_y \cos \theta}, \quad \tilde{u}_k = -\tan \theta \left(\bar{w}_k + \frac{\bar{u}_k(0)}{a_\xi} \right). \quad (4)$$

Since φ_k depends on J_y , which varies along the length, the warping-only deformation modes are moved from vector $\bar{\mathbf{u}}$ to $\tilde{\mathbf{u}}$, since the latter is multiplied by functions ϕ_k in Eq. (3). These additional or corrective warping deformation modes are shown in Fig. 1(d).

For convenience, the following vectors and matrices are defined

$$\mathbf{f} = \begin{bmatrix} \varphi \\ \phi \\ \varphi' \\ \phi' \\ \varphi'' \\ \phi'' \\ \varphi''' \\ \phi''' \end{bmatrix} = \mathcal{A}\Phi, \quad \Phi = \begin{bmatrix} \phi \\ \phi' \\ \phi'' \\ \phi''' \end{bmatrix}, \quad \mathcal{A} = \begin{bmatrix} 0 & \frac{1}{J_y \cos \theta} & 0 & 0 \\ 1 & 0 & 0 & 0 \\ 0 & \frac{\tan \theta}{a_\xi} & \frac{1}{J_y \cos \theta} & 0 \\ 0 & 1 & 0 & 0 \\ 0 & 0 & \frac{2 \tan \theta}{a_\xi} & \frac{1}{J_y \cos \theta} \\ 0 & 0 & 1 & 0 \end{bmatrix}. \quad (5)$$

This allows writing the mid-surface displacements as

$$\bar{\mathbf{U}} = \begin{bmatrix} U_X \\ U_y \\ U_a \end{bmatrix} = \Xi_{\bar{\mathbf{U}}}\mathbf{f}, \quad \Xi_{\bar{\mathbf{U}}} = \begin{bmatrix} \bar{\mathbf{u}}^T & \tilde{\mathbf{u}}^T & \mathbf{0} & \dots & \mathbf{0} \\ \mathbf{0} & \bar{\mathbf{v}}^T & \mathbf{0} & \dots & \mathbf{0} \\ \mathbf{0} & \bar{\mathbf{w}}^T & \mathbf{0} & \dots & \mathbf{0} \end{bmatrix}. \quad (6)$$

The strains require expressing the mid-surface displacements in local axes (x, y, z) , leading to

$$u = U_X \cos \theta + U_a \sin \theta, \quad v = U_y, \quad w = -U_X \sin \theta + U_a \cos \theta. \quad (7)$$

Then, using Kirchhoff's thin plate assumption, the linear strains are given by

$$\boldsymbol{\varepsilon} = \begin{bmatrix} \varepsilon_{xx} \\ \varepsilon_{yy} \\ \gamma_{xy} \end{bmatrix} = (\Xi_{\boldsymbol{\varepsilon}}^M + z\Xi_{\boldsymbol{\varepsilon}}^B)\mathbf{f}, \quad \Xi_{\boldsymbol{\varepsilon}}^M = \begin{bmatrix} J_x \cos \theta \bar{\mathbf{u}}_{,\xi}^T & J_x \bar{\boldsymbol{\omega}}_{,\xi}^T & \cos \theta \bar{\mathbf{u}}^T & \bar{\boldsymbol{\omega}}^T & \mathbf{0} & \mathbf{0} \\ \mathbf{0} & J_y \bar{\mathbf{v}}_{,\xi}^T & \mathbf{0} & \mathbf{0} & \mathbf{0} & \mathbf{0} \\ J_y \cos \theta \bar{\mathbf{u}}_{,\xi}^T & J_y \bar{\boldsymbol{\omega}}_{,\xi}^T + J_x \bar{\mathbf{v}}_{,\xi}^T & \mathbf{0} & \bar{\mathbf{v}}^T & \mathbf{0} & \mathbf{0} \end{bmatrix}, \quad (8)$$

$$\Xi_{\boldsymbol{\varepsilon}}^B = \begin{bmatrix} (J_{xx} \bar{\mathbf{u}}_{,\xi}^T + J_x^2 \bar{\mathbf{u}}_{,\xi\xi}^T) \sin \theta & (J_{xx} \bar{\boldsymbol{\omega}}_{,\xi}^T + J_x^2 \bar{\boldsymbol{\omega}}_{,\xi\xi}^T) & 2J_x \sin \theta \bar{\mathbf{u}}_{,\xi}^T & 2J_x \bar{\boldsymbol{\omega}}_{,\xi}^T & \sin \theta \bar{\mathbf{u}}^T & \bar{\boldsymbol{\omega}}^T \\ J_y^2 \bar{\mathbf{u}}_{,\xi\xi}^T \sin \theta & J_y^2 \bar{\boldsymbol{\omega}}_{,\xi\xi}^T & \mathbf{0} & \mathbf{0} & \mathbf{0} & \mathbf{0} \\ 2(J_{xy} \bar{\mathbf{u}}_{,\xi}^T + J_y J_x \bar{\mathbf{u}}_{,\xi\xi}^T) \sin \theta & 2(J_{xy} \bar{\boldsymbol{\omega}}_{,\xi}^T + J_y J_x \bar{\boldsymbol{\omega}}_{,\xi\xi}^T) & 2J_y \sin \theta \bar{\mathbf{u}}_{,\xi}^T & 2J_y \bar{\boldsymbol{\omega}}_{,\xi}^T & \mathbf{0} & \mathbf{0} \end{bmatrix}, \quad (9)$$

with $\bar{\boldsymbol{\omega}}_k = \cos \theta \tilde{\boldsymbol{\omega}}_k + \sin \theta \bar{\boldsymbol{w}}_k$ and $\boldsymbol{\omega}_k = \sin \theta \tilde{\boldsymbol{\omega}}_k - \cos \theta \bar{\boldsymbol{w}}_k$.

Since a linearized stability analysis is sought, rather than a full geometrically non-linear analysis, only the linearization (Δ) of the virtual variation (δ) of the Green-Lagrange strains is required. Due to the thin-walled nature of the beam, only the non-linear membrane terms are retained, reading

$$\Delta \delta E_{ij}^{NLM} = \delta \mathbf{f}^T \Xi_{D^2 E_{ij}}^{NLM} \Delta \mathbf{f}, \quad \Xi_{D^2 E_{ij}}^{NLM} = a_{ij} \mathbf{A} + b_{ij} \mathbf{B} + c_{ij} \mathbf{C}, \quad (10)$$

where matrices \mathbf{A} - \mathbf{C} are symmetric and composed of 6×6 blocks $(\cdot)^{(ij)}$ of dimension $D \times D$. The non-null blocks of the upper triangle of these matrices read

$$\begin{cases} \mathbf{A}^{(1,1)} = \bar{\mathbf{u}}_{,\xi} \bar{\mathbf{u}}_{,\xi}^T, & \mathbf{A}^{(1,2)} = \bar{\mathbf{u}}_{,\xi} \tilde{\mathbf{u}}_{,\xi}^T, & \mathbf{A}^{(2,2)} = \tilde{\mathbf{u}}_{,\xi} \tilde{\mathbf{u}}_{,\xi}^T + \bar{\mathbf{v}}_{,\xi} \bar{\mathbf{v}}_{,\xi}^T + \bar{\mathbf{w}}_{,\xi} \bar{\mathbf{w}}_{,\xi}^T, \\ \mathbf{B}^{(1,3)} = \bar{\mathbf{u}}_{,\xi} \bar{\mathbf{u}}^T, & \mathbf{B}^{(2,3)} = \tilde{\mathbf{u}}_{,\xi} \bar{\mathbf{u}}^T, & \mathbf{B}^{(2,4)} = \tilde{\mathbf{u}}_{,\xi} \tilde{\mathbf{u}}^T + \bar{\mathbf{v}}_{,\xi} \bar{\mathbf{v}}^T + \bar{\mathbf{w}}_{,\xi} \bar{\mathbf{w}}^T, & \mathbf{B}^{(1,4)} = \bar{\mathbf{u}}_{,\xi} \tilde{\mathbf{u}}^T, \\ \mathbf{C}^{(3,3)} = \bar{\mathbf{u}} \bar{\mathbf{u}}^T, & \mathbf{C}^{(3,4)} = \bar{\mathbf{u}} \tilde{\mathbf{u}}^T, & \mathbf{C}^{(4,4)} = \tilde{\mathbf{u}} \tilde{\mathbf{u}}^T + \bar{\mathbf{v}} \bar{\mathbf{v}}^T + \bar{\mathbf{w}} \bar{\mathbf{w}}^T, \end{cases} \quad (11)$$

and the coefficients a_{ij} - c_{ij} are provided in Table 1. It should be noted that the equations for the prismatic case are recovered exactly with the present ones with $J_x = \theta = \tilde{u}_{,k} = 0$ (Gonçalves & Camotim 2012).

Table 1: Coefficients a_{ij} - c_{ij}

Component	E_{xx}	E_{yy}	$2E_{xy}$
a_{ij}	J_x^2	J_x^2	$2J_x J_y$
b_{ij}	J_x	0	J_y
c_{ij}	1	0	0

3.2 Stress and equilibrium

A plane stress state is assumed, with the second Piola-Kirchhoff stresses $\mathbf{S}^T = [S_{xx} \ S_{yy} \ S_{xy}]$ decomposed into membrane and bending terms, $\mathbf{S} = \mathbf{S}^M + \mathbf{S}^B$. A St. Venant-Kirchhoff material is assumed, defined by Young's modulus E , Poisson's ratio ν and the shear modulus G . The stresses are obtained from the strains using $\mathbf{S}^M = \mathbf{C}^M \mathbf{E}^M$ and $\mathbf{S}^B = \mathbf{C}^B \mathbf{E}^B$, with

$$\mathbf{C}^B = \mathbf{C}^M = \begin{bmatrix} \frac{E}{1-\nu^2} & \frac{\nu E}{1-\nu^2} & 0 \\ \frac{\nu E}{1-\nu^2} & \frac{E}{1-\nu^2} & 0 \\ 0 & 0 & G \end{bmatrix} \quad \text{or} \quad \mathbf{C}^M = \begin{bmatrix} E & 0 & 0 \\ 0 & 0 & 0 \\ 0 & 0 & G \end{bmatrix}, \quad (12)$$

where the latter case applies if $E_{yy}^M = 0$ is assumed, to prevent overly stiff solutions.

The equilibrium equations are obtained using virtual work. For the linear case, one writes

$$\int_L \delta \mathbf{f}^T \left[\underbrace{- \int_{S_\xi} (\mathbf{\Xi}_\varepsilon^M)^T \mathbf{C}^M \mathbf{\Xi}_\varepsilon^M \frac{t}{J_y} d\xi}_{\mathcal{M}^M} - \underbrace{\int_{S_\xi} \frac{t^3}{12J_y} (\mathbf{\Xi}_\varepsilon^B)^T \mathbf{C}^B \mathbf{\Xi}_\varepsilon^B d\xi}_{\mathcal{M}^B} + \lambda \underbrace{\int_{S_\xi} \mathbf{\Xi}_\bar{v}^T \bar{\mathbf{q}} \frac{1}{J_y} d\xi}_{\mathcal{F}} \right] dx = 0, \quad (13)$$

where t is the tube thickness, S_ξ is the mid-line of the parent cross-section, $\bar{\mathbf{q}}$ are surface loads acting along the (X, y, a) axes and λ is the load parameter. A linear stability analysis requires a linear step to evaluate the pre-buckling membrane stresses \mathbf{S}^M , and a second step for the calculation of the non-trivial solutions of the buckling eigenvalue problem

$$\int_L \delta \mathbf{f}^T [\mathcal{M}^M + \mathcal{M}^B + \lambda \mathcal{G}(\mathbf{S})] \Delta \mathbf{f} dx = 0, \quad (14)$$

with the geometric matrix

$$\mathcal{G}(\mathbf{S}) = \frac{t}{J_y} \int_{S_\xi} \left(S_{xx}^M \mathbf{\Xi}_{D^2 E_{xx}}^{NLM} + S_{yy}^M \mathbf{\Xi}_{D^2 E_{yy}}^{NLM} + S_{xy}^M \mathbf{\Xi}_{D^2 2E_{xy}}^{NLM} \right) d\xi. \quad (15)$$

3.3 The displacement-based finite element

A standard GBT displacement-based element is obtained introducing the interpolation $\boldsymbol{\phi} = \mathbf{N} \mathbf{d}_e$, where matrix \mathbf{N} collects the interpolation functions — Hermite cubic functions — and vector \mathbf{d}_e collects their nodal values. This leads to

$$\Phi = \mathcal{N}d_e, \quad \mathcal{N} = \begin{bmatrix} N \\ N' \\ N'' \\ N''' \end{bmatrix}. \quad (16)$$

The element linear and geometric stiffness matrices, and the external load vector, read

$$\mathbf{K}_e = \int_{L_e} (\mathcal{A}\mathcal{N})^T (\mathcal{M}^M + \mathcal{M}^B) \mathcal{A}\mathcal{N} dx, \quad (17)$$

$$\mathbf{G}_e = \int_{L_e} (\mathcal{A}\mathcal{N})^T \mathcal{G} \mathcal{A}\mathcal{N} dx, \quad (18)$$

$$\mathbf{F}_e = \lambda \int_{L_e} (\mathcal{A}\mathcal{N})^T \mathcal{F} dx, \quad (19)$$

The integrations are carried out with 3 Gauss points along x and $3(m + 1)$ Gauss points along ξ in each wall. The finite element analysis was implemented in MATLAB (The MathWorks, 2024).

4. Numerical examples

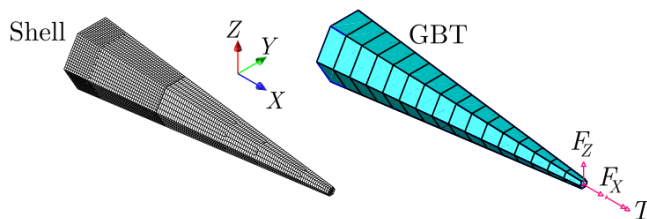
In the examples presented next, consistent units are used, with $E = 210000$ and $\nu = 0.3$. The initial apothem is fixed at $a_0 = 2$, while the remaining parameters are varied. For comparison and validation purposes, solutions obtained with refined meshes of MITC4 shell elements in ADINA (Bathe, 2019) are reported. The percentage differences provided are calculated with respect to the shell solution. The GBT results correspond to uniform and converged meshes, in the sense that several analyses are sequentially carried out, doubling the number of elements at each step or the number of intermediate nodes, whichever is most appropriate, and considering the mesh converged when the next step changes the result by less than 0.1%. The GBT and shell discretizations are provided in each figure. The number of DOFs equals $2D(NFE + 1)$ for the GBT models and approximately $5NFE$ for the shell models.

4.1 First-order analysis

A set of linear problems is first presented. In all these problems the $X = 0$ end section is fixed. It is recalled that the deformation modes for $n = 6$ are shown in Fig. 1. In the GBT solution, “RB” stands for the rigid-body modes, “D” for the distortional modes and “LP” for the local-plate modes.

Figs. 2-5 display the results for the linear problems, namely the GBT and shell deformed configurations, and the GBT mode amplitude diagrams. Fig. 2 concerns a thick tube undergoing global deformation (axial-bending-torsion), while the remaining results mostly concern distortional deformation, except the last case in Fig. 5, which involves local-plate deformation. Figs. 3-4 show results for long and short tubes, characterized by the slenderness parameter $\lambda = L_X/2a(L/2)$ — L_X is the length along X , thus $L_X = L/\cos\theta$, and $a(L/2)$ is the average apothem —, and subjected to a uniformly distributed load applied perpendicularly to the fold, hence having a component along Y and, for the tapered case, also along X . In Fig. 5 concentrated loads are applied instead. In all cases an excellent GBT-shell match is found even for high taper angles. It is quite remarkable that in general just a few deformation modes participate in the solution. Nevertheless, for the most complex cases, which involve a high taper angle, it is necessary to use more GBT finite elements and include all deformation modes in the analysis.

$$\begin{aligned}\theta &= -5^\circ \\ t &= 0.02 \\ L &= 20\end{aligned}$$



	$F_X = 1$		$F_Z = 1$		$T = 1$	
	No. of elements	X displ.	No. of elements	Z displ.	No. of elements	X rotation
Shell	5232	8.150E-4	5232	7.586E-4	5232	7.621E-3
GBT	4	8.153E-4 (0.0%)	8	7.474E-4 (1.5%)	4	7.613E-3 (0.1%)

Figure 2: Linear analysis of a long and thick tube subjected to global deformation.

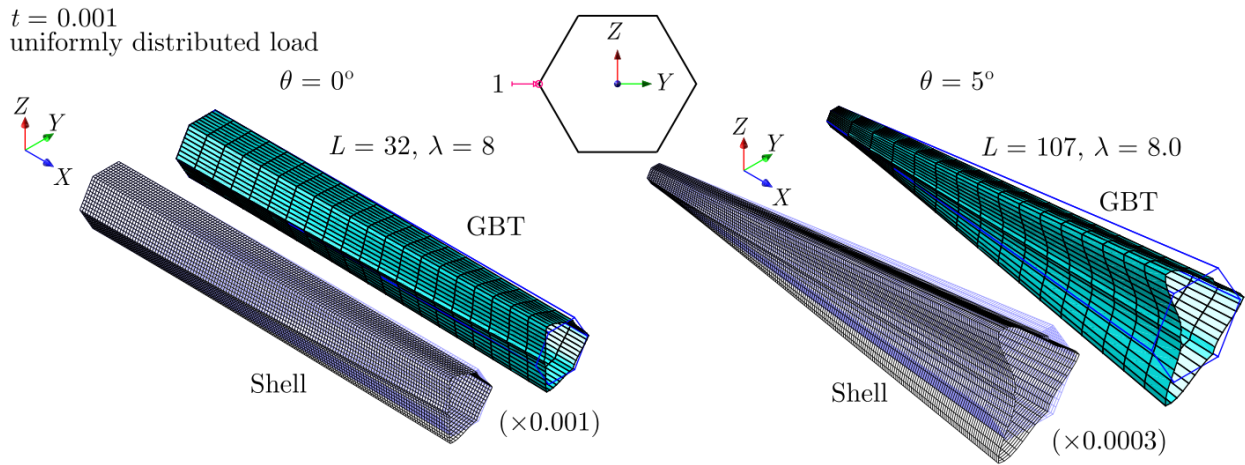
4.2 Buckling analysis

This section concerns the calculation of bifurcation loads and buckling modes. For the prismatic case the adopted length is $L_X = 20$, while the remaining parameters were chosen to allow capturing the relevant phenomena — global, distortional and local buckling —, using the formulas and graphs provided in Gonçalves & Camotim (2013b, 2013c). For the tapered case the geometry was adjusted to allow capturing the same phenomena, while keeping the a_0 value and the minimum apothem always above 0.25.

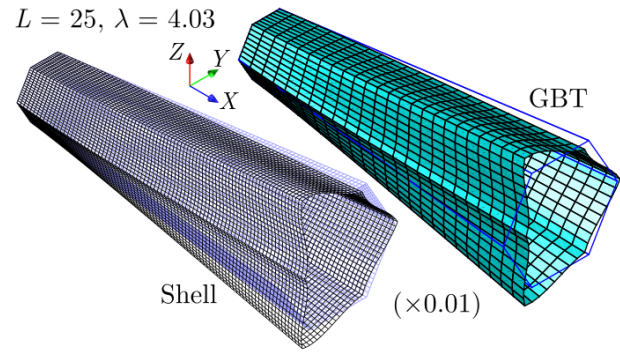
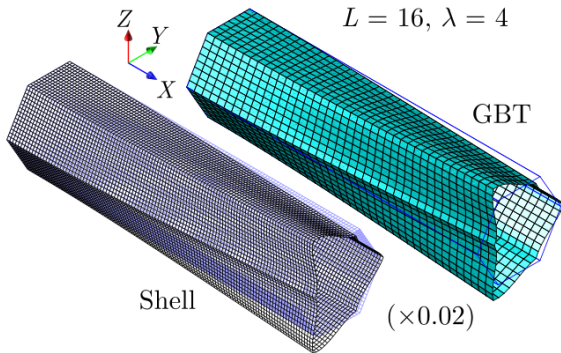
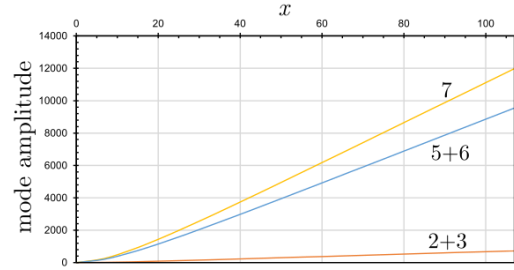
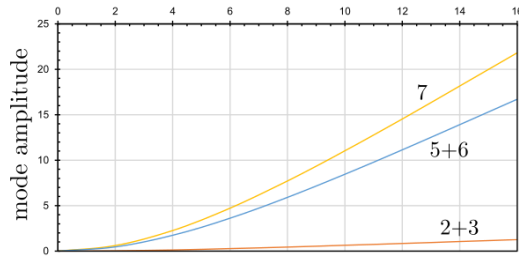
The shell results are obtained for converged meshes: a maximum element length of 0.2 is first considered, and then sequentially halved until the change in the critical load is below 0.1 %. The end sections have diaphragms that restrain the wall displacements, not the rotations except where mentioned, and are simply supported. In the shell models this requires adding rigid links (for displacement DOFs and where appropriate rotation DOFs) between the cross-section nodes and the centroid. In the GBT models this is achieved through (i) $\phi_k = 0$ for all modes except the shear counterparts to bending and, at the end where the load is applied, also except for the axial extension and torsion modes, and (ii) $\phi'_k = 0$ for the distortional modes, otherwise differential warping at the end sections would be allowed.

The results are reported in Figs. 6-8, for tubes under axial compression, and Figs. 9-10, for tubes under torsion. Each figure concerns a particular buckling type and shows the critical bifurcation loads obtained with both models (GBT and shell), the corresponding buckling modes and the GBT mode amplitude graphs. It is recalled that, when two modes are obtained, any combination of them also constitutes a valid buckling mode. In these situations only one mode amplitude graph is provided, as this suffices to grasp the buckling mode nature. It is also recalled that the deformation modes for $n = 6, m = 2$ are shown in Fig. 1; for other cases the relevant deformation modes are displayed in the mode amplitude graphs.

In all cases GBT leads to very accurate results with a relatively small number of finite elements, and only a few deformation modes participate in the buckling mode. It is worth remarking that the GBT analyses are quite fast, even though the GBT finite element procedure was implemented in MATLAB. For instance, in the $\theta = -20^\circ$ case in Fig. 10, the runtime of the shell and GBT models (for converged meshes) is 125 and 3.5 seconds, respectively. In the next paragraphs, attention is called to specific aspects of these results.



	Number of elements	Maximum Y displacement	Number of elements	Maximum Y displacement
Shell	8700	695.9	8592	25247
GBT, RB+D	2	693.3 (0.4%)	16	25369 (-0.5%)



	Number of elements	Maximum Y displacement	Number of elements	Maximum Y displacement
Shell	9630	46.99	7968	174.4
GBT, RB+D	2	45.45 (3.3%)	8	169.3 (2.9%)

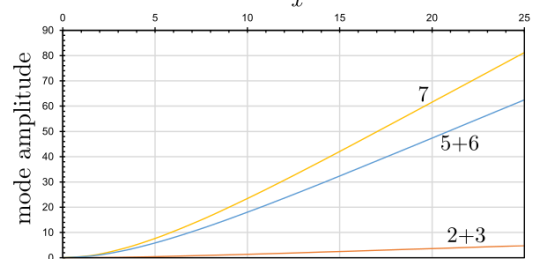
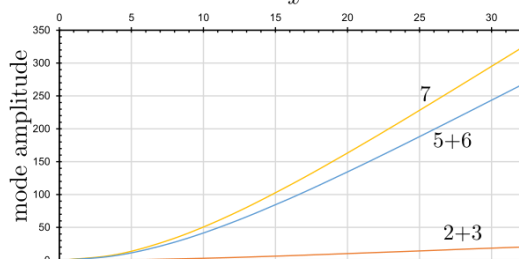


Figure 3: Linear analysis of long tubes subjected to a uniformly distributed lateral load.

$t = 0.001$
uniformly distributed load

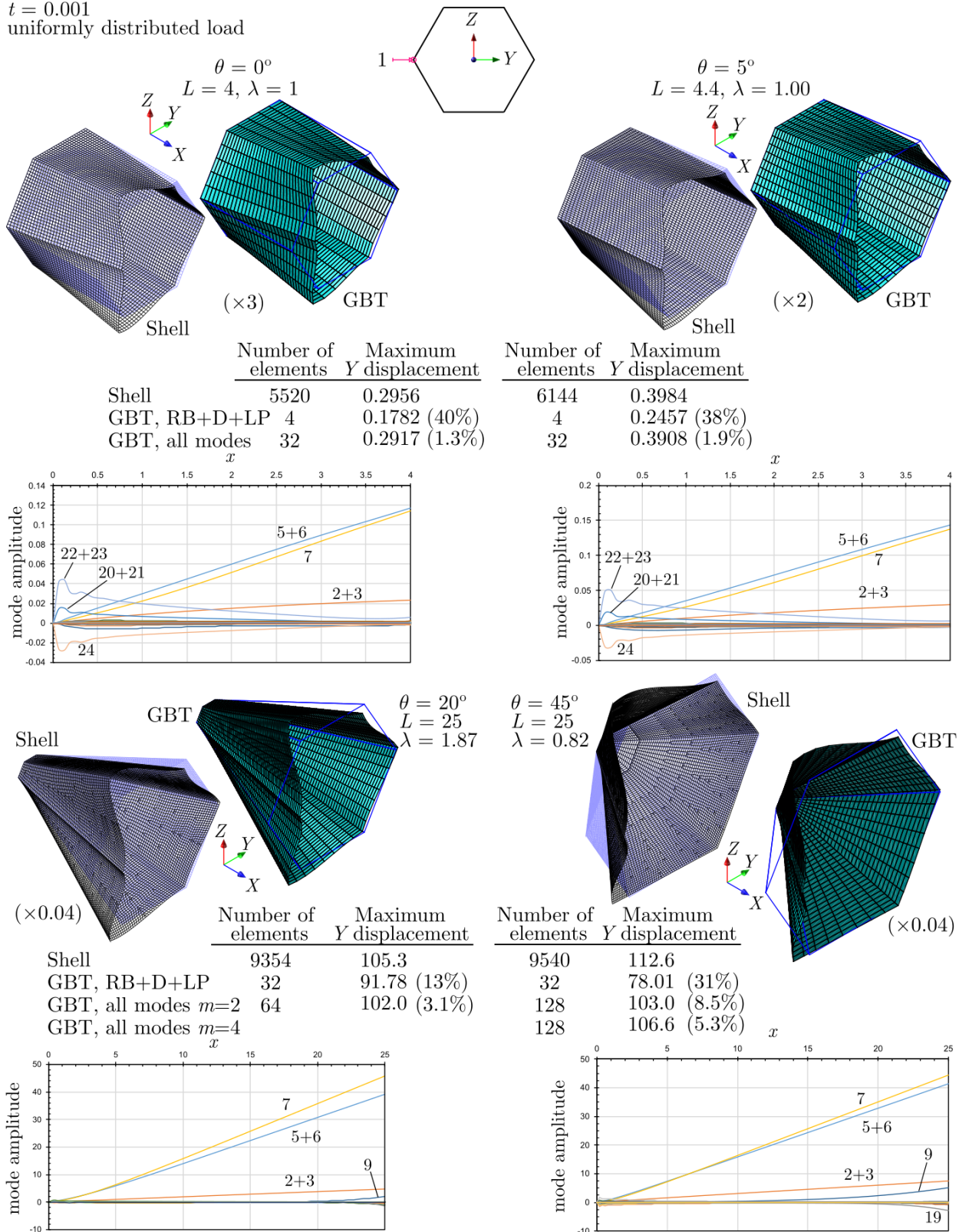
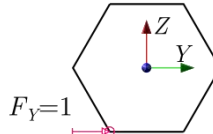
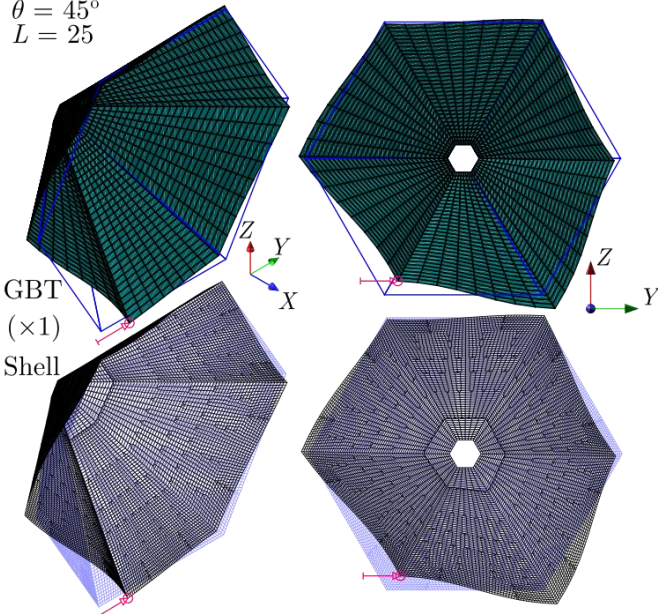


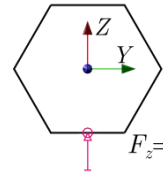
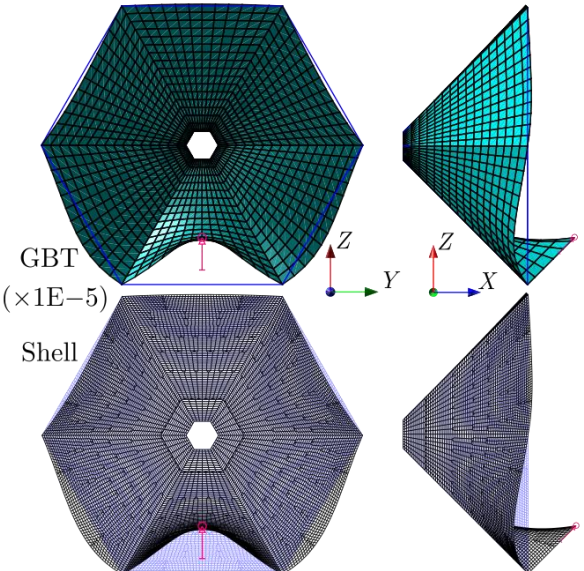
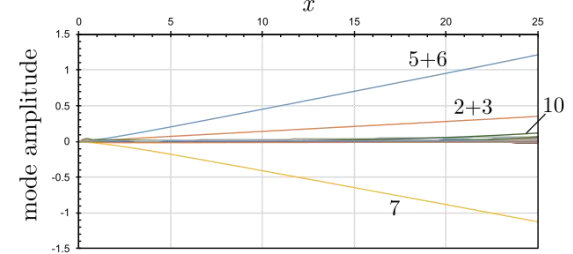
Figure 4: Linear analysis of short tubes subjected to a uniformly distributed lateral load.

$t = 0.001$
 concentrated force
 $\theta = 45^\circ$
 $L = 25$



Number of elements Load point Y displacement

Shell	9780	3.344
GBT, RB+D+LP	32	2.509 (25%)
GBT, all modes	64	3.206 (2.5%)



$F_z = -1$ ($F_x = F_z = \sqrt{2}/2$)

Number of elements Load point X displ. Z displ.

Shell	9780	6.766E5	6.766E5
GBT, $m=2$	4	5.635E5 (16%)	5.635E5 (16%)
GBT, $m=3$ (RB+D+LP)	4	6.664E5 (1.5%)	6.664E5 (1.5%)

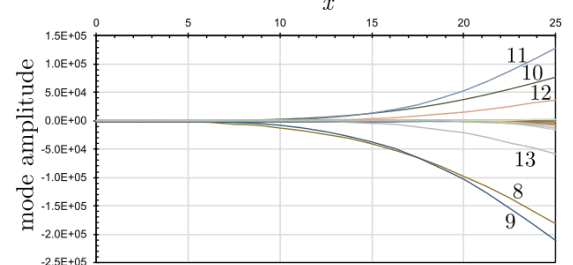


Figure 5: Linear analysis of short tubes subjected to concentrated loads.

For flexural (global) buckling under compression (Fig. 6), two buckling modes with the same critical load are obtained, since all central axes are principal (only one buckling mode is shown). For the prismatic case the Euler buckling load is approximately 30 % above the shell and GBT bifurcation loads reported, since the tube is relatively short and thus shear deformation plays a non-negligible role. This is visible in the GBT mode amplitude graph, in the presence of modes 20+21, which account for about 25 % of the difference with respect to the Euler load, while the remaining 5 % stem from the non-linear strain term due to warping, see Gonçalves et al. (2010).

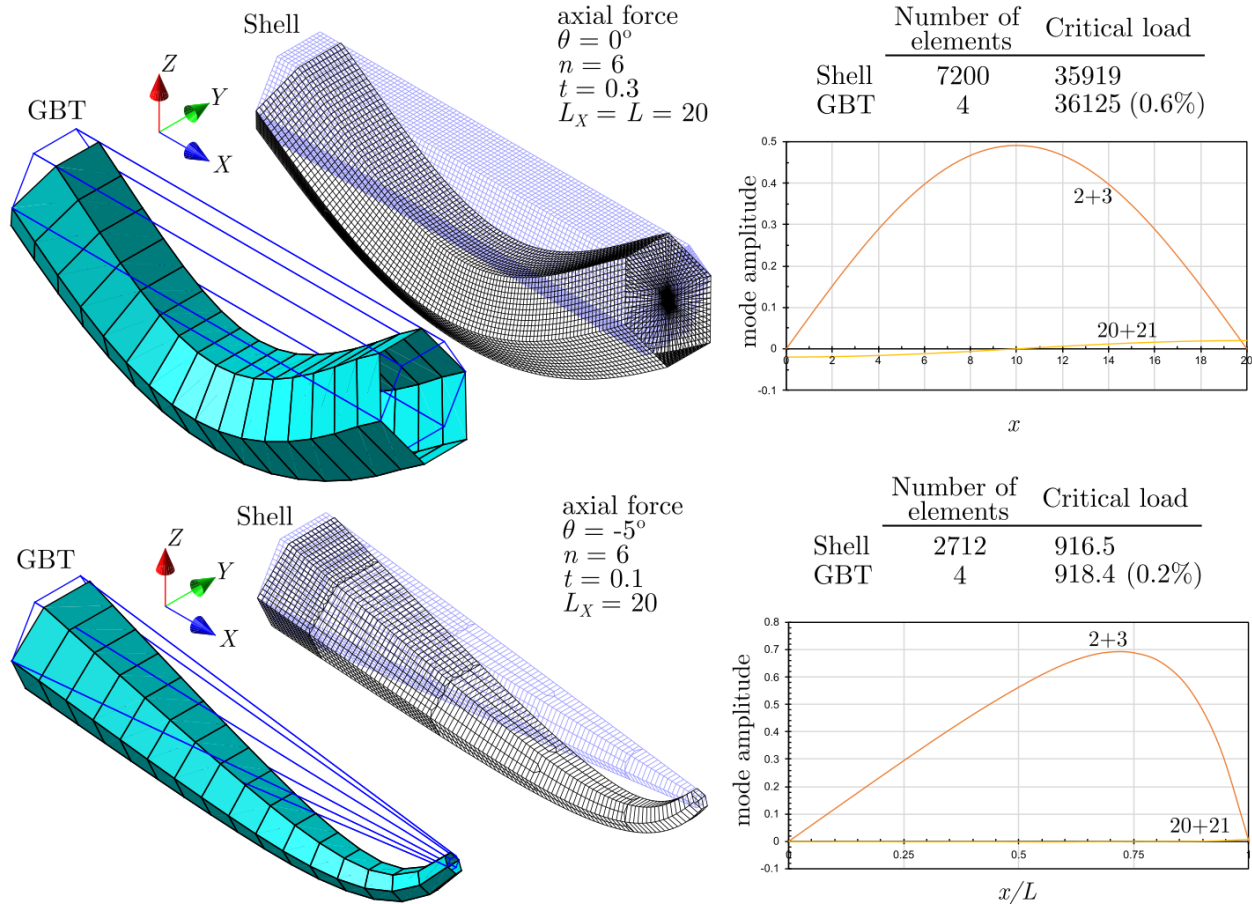


Figure 6: Flexural buckling of tubes under compression.

For the tapered case an asymmetric buckle leaning towards the narrow end is observed, the slender part of the tube. The same deformation modes are triggered, but the shear modes influence the critical load by only 7 %.

For local buckling under compression, see Fig. 7, the GBT solution features exclusively the local-plate deformation mode 8. For the prismatic case the critical load is close to the analytical solution for infinitely long simply supported plates $\sigma_{cr} = 4\pi^2 E(t/b)^2/12(1 - \nu^2)$, leading to $N_{cr} = 1972$. For the tapered case local buckling occurs at the wider end, since the critical load is inversely proportional to b . This is clearly visible in the buckling modes and mode amplitude graphs. Using the solution for simply supported plates leads to errors that increase with the taper angle (7 % for $\theta = -5^\circ$, 17 % for $\theta = -20^\circ$). For $\theta = -45^\circ$ it was necessary to increase the number of intermediate nodes to 3, otherwise the differences with respect to the shell model reach 10 %.

For distortional buckling under compression, Fig. 8, for $n = 12$ the end diaphragms also restrain the wall rotations, to avoid local buckling. Two critical buckling modes are obtained, corresponding to the deformation mode pair 7-8, together with its shear pair counterpart 30-31 and the local-plate pair 19-20. As the taper angle increases, the influence of the shear and local-plate modes increases. Moreover, the number of shell elements required to obtain converged results increases significantly, while the GBT solution requires much less elements. Interestingly, in the tapered case, the distortional buckles are more pronounced in the narrow zone.

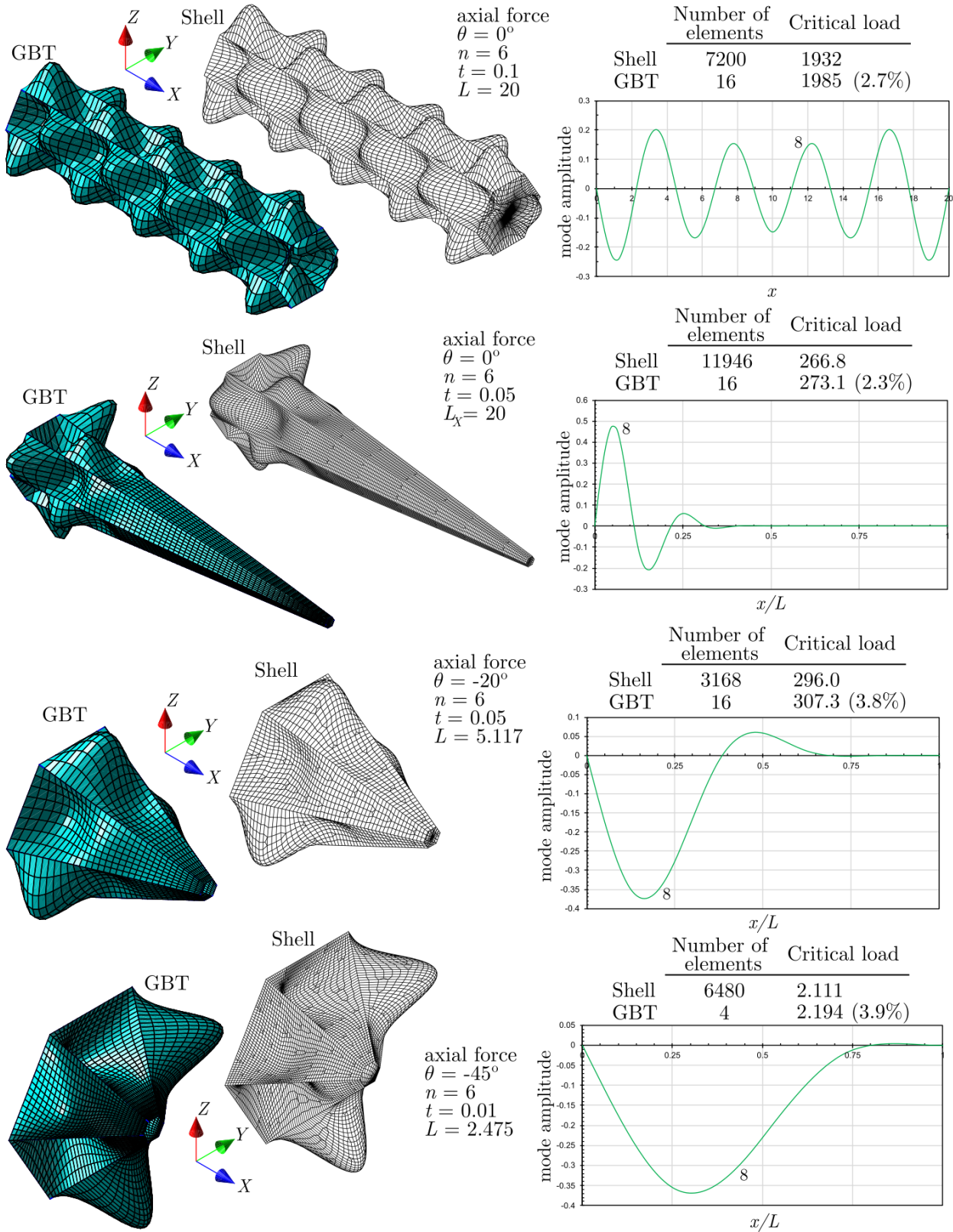


Figure 7: Local buckling of tubes under compression.

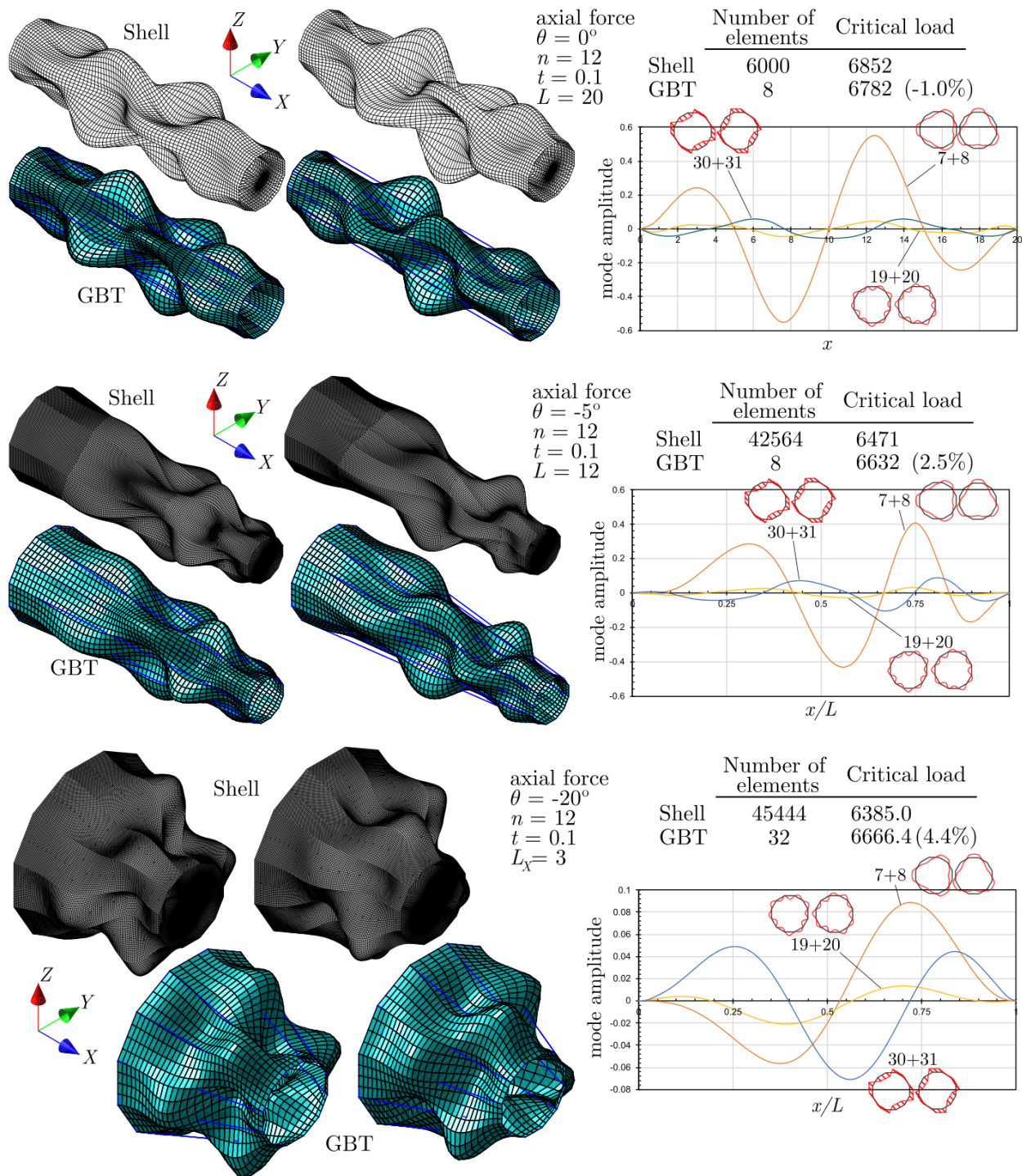


Figure 8: Distortional buckling of tubes under compression.

For distortional buckling under torsion, Fig. 9, very refined shell models are required, while only 8 GBT elements suffice and very few deformation modes are triggered. A mixed distortional-local buckling mode is obtained, essentially involving deformation modes 7 (distortional) and 8 (local), with small participations of modes 19 (local) and 24 (the shear counterpart to mode 7). Note also that, for the tapered case, the buckles move towards the narrow zone.

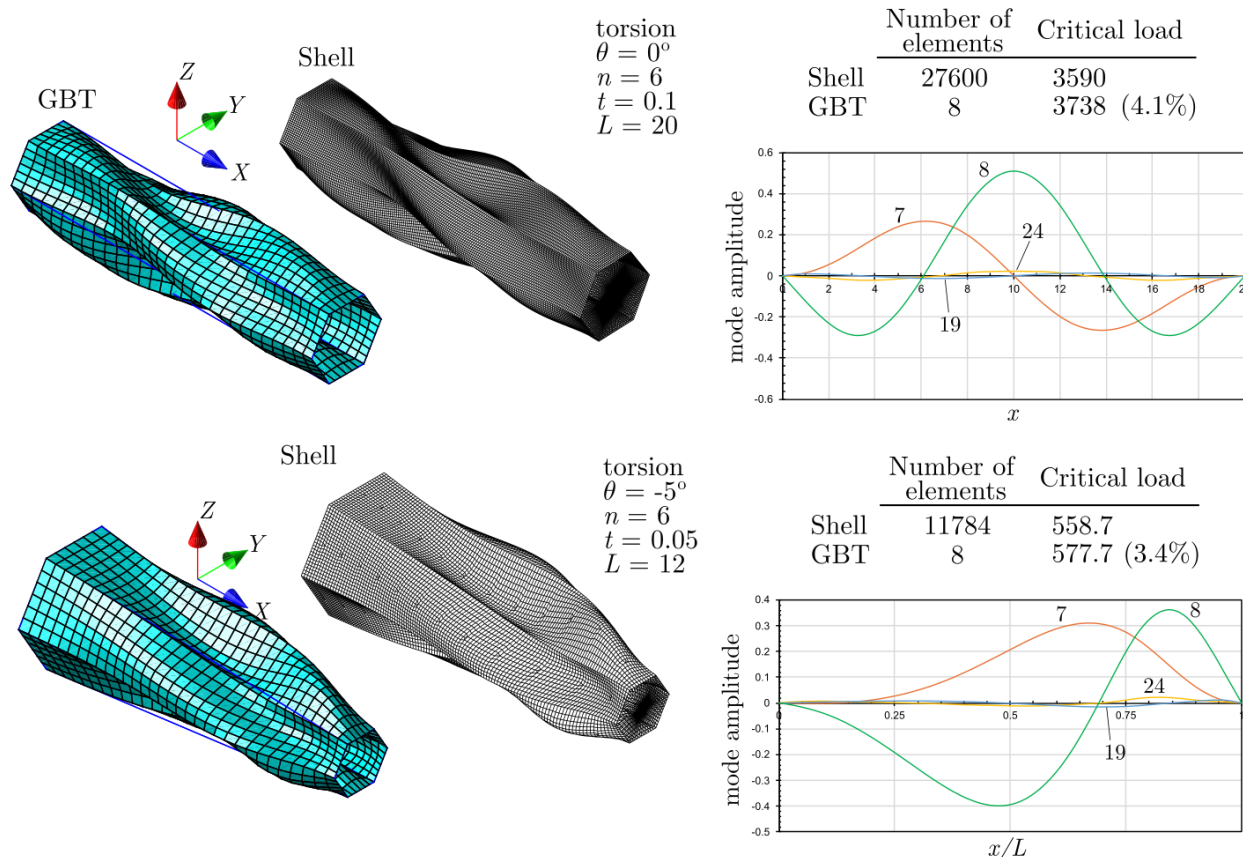


Figure 9: Distortional buckling of tubes under torsion.

Finally, Fig. 10 shows results for local buckling under torsion, in which case two critical buckling modes are always obtained. The GBT solution only involves the local-plate modes. Very refined shell meshes are required for the two most tapered cases, while only 8 GBT elements suffice. However, in both cases the GBT solution requires all deformation modes (not just the conventional ones) and three intermediate nodes, otherwise the critical load falls 11-12 % above the shell value.

5. Conclusions

This paper presented and validated a GBT extension for tapered RCPS tubes, which makes it possible to calculate global-distortional-local bifurcation loads and buckling modes according to the linear stability analysis concept. The proposed formulation assumes a genuinely tapered member and includes all non-linear membrane terms of the Green-Lagrange strains, without further simplifying assumptions. Since the deformation mode families of the prismatic GBT are used, the formulation inherits the unique GBT modal decomposition features, which allow an in-depth characterization of the nature of the buckling modes. Although the formulation is quite involved, due to the tapered geometry, all expressions required to implement a displacement-based finite element were provided in a simple vector-matrix format. The numerical examples presented show that the proposed approach leads to very accurate first-order and buckling results, even for tubes having taper angles up to 45° , with a very small computational cost.

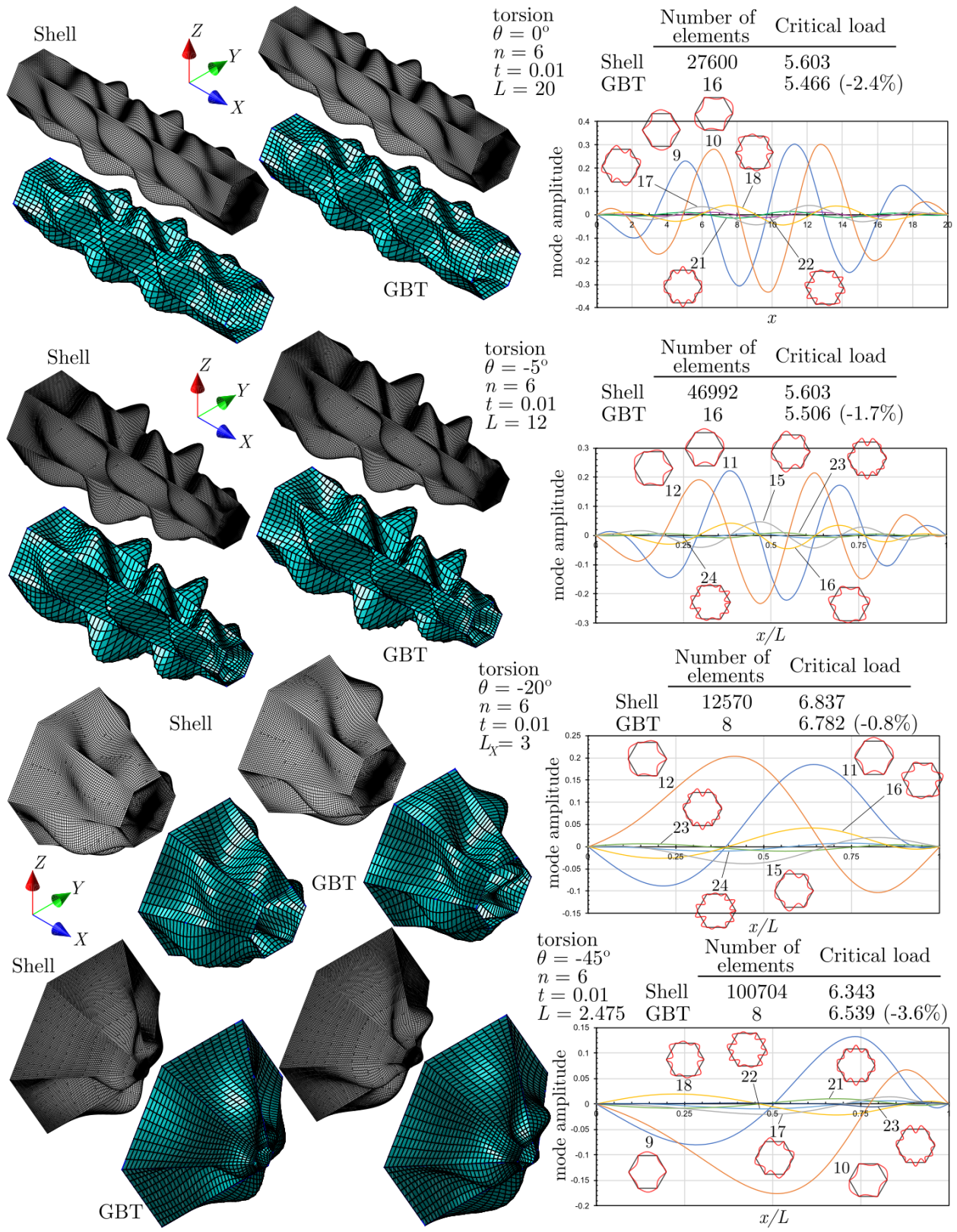


Figure 10: Local buckling of tubes under torsion.

Acknowledgments

This work is part of the research activity carried out at Civil Engineering Research and Innovation for Sustainability (CERIS) and has been funded by Fundação para a Ciência e a Tecnologia (FCT) in the framework of project UIDB/04625/2020.

References

- Bathe, K. (2019). *ADINA System*, ADINA R&D Inc.
- Bebiano, R., Gonçalves, R., Camotim, D. (2015). “A cross-section analysis procedure to rationalise and automate the performance of GBT-based structural analyses.” *Thin-Walled Structures*, 92 29-47.
- Bebiano, R., Camotim, D., Gonçalves, R., (2018). “GBTUL 2.0 – a second-generation code for the GBT-based buckling and vibration analysis of thin-walled members.” *Thin-Walled Structures*, 124 235-253.
- Gonçalves, R., Le Grogneq, P., Camotim, D. (2010). “GBT-based semi-analytical solutions for the plastic bifurcation of thin-walled members.” *International Journal of Solids and Structures*, 47 (1) 34-50.
- Gonçalves, R., Camotim D. (2011). “GBT-based finite elements for elastoplastic thin-walled metal members.” *Thin-Walled Structures*, 49 (10) 1237-1245.
- Gonçalves, R., Camotim, D. (2012). “Geometrically non-linear Generalised Beam Theory for elastoplastic thin-walled metal members.” *Thin-Walled Structures*, 51 121-129.
- Gonçalves, R., Camotim, D. (2013a). “On the behaviour of thin-walled steel regular polygonal tubular members.” *Thin-Walled Structures*, 62 191-205.
- Gonçalves, R., Camotim, D. (2013b). “Elastic buckling of uniformly compressed thin-walled regular polygonal tubes.” *Thin-Walled Structures*, 71 35-45.
- Gonçalves, R., Camotim, D. (2013c). “Buckling behaviour of thin-walled regular polygonal tubes subjected to bending or torsion.” *Thin-Walled Structures*, 73 185-197.
- Gonçalves, R., Camotim, D. (2014). “The vibration behaviour of thin-walled regular polygonal tubes.” *Thin-Walled Structures*, 84 177-188.
- Gonçalves, R., Nedelcu, M. (2024). “First-order GBT for truncated conical shells with circular cross-section.” *Thin-Walled Structures*, 112210.
- Gonçalves, R. (2025). “First-order GBT for tapered regular convex polygonal tubes.” *Thin-Walled Structures*, 207, 112735.
- Martins, A.D., Camotim, D., Gonçalves, R., Dinis, P. (2018). “Enhanced geometrically nonlinear generalized beam theory formulation: Derivation, numerical implementation, and illustration.” *Journal of Engineering Mechanics*, 144 (6) 04018036.
- Martins, A.D., Gonçalves, R., Camotim, D. (2019a). “On the local and distortional post-buckling behaviour of thin-walled regular polygonal tubular columns.” *Thin-Walled Structures*, 138 46-63.
- Martins, A.D., Gonçalves, R., Camotim, D. (2019b). “Post-buckling behaviour of thin-walled regular polygonal tubular columns undergoing local-distortional interaction.” *Thin-Walled Structures*, 138 373-391.
- Martins, A.D., Gonçalves, R., Camotim, D. (2021). “Post-buckling behaviour of thin-walled regular polygonal tubes subjected to bending.” *Thin-Walled Structures*, 166 108106.
- The MathWorks Inc. (2024). MATLAB Version R2024b, Massachusetts.
- Nedelcu, M. (2011). “GBT formulation to analyse the buckling behaviour of isotropic conical shells.” *Thin-Walled Structures*, 49 (7) 812-818.
- Mureşan, A.-A., Nedelcu, M., Gonçalves, R. (2019). “GBT-based FE formulation to analyse the buckling behaviour of isotropic conical shells with circular cross-section.” *Thin-Walled Structures*, 134 84-101.
- Schardt, R. (1989). *Verallgemeinerte Technische Biegetheorie*, Berlin, Springer Verlag.